



# Formation of H<sub>2</sub>O in the CH<sub>4</sub>-CO<sub>2</sub> dry reforming process and its activation to this reaction over Ni-Fe/MC12A7 catalysts

Lingxiang Huang<sup>a,b,c</sup>, Yue Ma<sup>a,b,c</sup>, Mufan Niu<sup>a,b,c</sup>, Shenyong Ren<sup>a,b,c</sup>, Qiaoxia Guo<sup>d</sup>, Chunming Xu<sup>a,b,c</sup>, Baojian Shen<sup>a,b,c,\*</sup>

<sup>a</sup> College of Chemical Engineering and Environment, China University of Petroleum, No. 18 Fuxue Road, Changping, Beijing 102249, China

<sup>b</sup> The Key Laboratory of Catalysis of CNPC, Beijing 102249, China

<sup>c</sup> State Key Laboratory of Heavy Oil Processing, China University of Petroleum, No. 18 Fuxue Road, Changping, Beijing 102249, China

<sup>d</sup> College of Science, China University of Petroleum, No. 18 Fuxue Road, Changping, Beijing 102249, China

## ARTICLE INFO

### Keywords:

C12A7-O<sup>2-</sup>

CO<sub>2</sub> adsorption

H<sub>2</sub>O formation and inducing effect

Isotope <sup>13</sup>CH<sub>4</sub> tracing

Remove carbon deposition

## ABSTRACT

Dry reforming reaction of greenhouse gas CH<sub>4</sub> and CO<sub>2</sub> was studied over Ni-Fe bimetallic catalyst, in which the composite support of C12A7-O<sup>2-</sup> in MCM-41 was used. The isotope <sup>13</sup>CH<sub>4</sub>/D<sub>2</sub>O tracing experiment showed CO mainly comes from <sup>13</sup>CH<sub>x</sub> oxidation reaction and DH comes from CH<sub>x</sub> and D<sub>2</sub>O reaction, exhibiting lattice oxygen promotes CH<sub>x</sub> oxidation and water accelerate methane conversion. XPS and TPSR-MS studies exhibited the existence of lattice oxygen in catalysts produces a little H<sub>2</sub>O to facilitate a lower starting point at the reaction temperature. On-line MS investigation found that the trace water addition in the system accelerated the adsorption of CO<sub>2</sub> on support and promoted methane dissociation, the H<sub>2</sub> signal appears later than CO, indicating the oxidation reaction of CH<sub>x</sub> occurs after the dissociation of CO<sub>2</sub>. Besides, TG analysis tells us the H<sub>2</sub>O may consume Ca on the catalyst in time during the reaction process to remove carbon deposition.

## 1. Introduction

The conversion of methane and carbon dioxide is significant because they are the main greenhouse gases. Dry reforming of methane (DRM) can convert CO<sub>2</sub> and CH<sub>4</sub> into syngas, which can further be transformed into liquid fuels or other chemicals through Fischer-Tropsch synthesis (FTS) [1–3]. The main research on methane carbon dioxide reforming focuses on Ni-based catalysts system, due to nickel more abundant and cheaper [4–6]. However, one of the biggest challenges is that Ni catalysts are easy to agglomerate into the Ni clusters, resulting in catalyst deactivation through the blocking of the catalyst pores [7–13]. In addition, methane cracking (CH<sub>4</sub> = C + 2 H<sub>2</sub>) becomes more thermodynamically favorable at high temperatures. Boudouard reaction (2CO = CO<sub>2</sub> + C) is prone to occur below 973 K, and carbon deposition is more serious at the temperature of the reforming reaction. Therefore, the agglomeration of active components at high temperature and a large amount of carbon deposition on the catalyst surface leading to deactivation is an urgent problem to be solved. In order to solve the above problems, the effects of supports, promoters, and other metals have been

extensively studied. In supported catalysts, some supports (such as Al<sub>2</sub>O<sub>3</sub>, SiO<sub>2</sub>, MgO, SBA-15) can effectively participate in the reaction in addition to a supporting role and prevent carbon deposition [14–17]. Besides, some supports can effectively delay carbon deposition of catalysts. Peng et al. reported Ni-Fe/mayenite catalysts exhibited higher activity and stability in methane carbon dioxide reforming [18]. The unique unit cell structure of mayenite (C12A7) contains twelve positively charged cages and two free cations randomly occupying the cage center [19]. These free oxygen ions can migrate further on the support and react with carbon deposition to form CO, which improves the stability of the catalyst. However, the small specific surface area of the mayenite (~10 m<sup>2</sup>/g) support limits the carbon capacity of the catalyst [20]. Mahadi et al. reported the effect of mesoporous alumina structure on methane reforming reaction. The high specific surface area and ordered mesopores of the catalyst support improved the reactive activity [21]. Shamska studied that NiO-Al<sub>2</sub>O<sub>3</sub> catalysts were synthesized by ultrasound-assisted coprecipitation method and showed high activity with a low degree of carbon formation [22]. Li et al. ordered different architectures of mesoporous SiC materials which they prepared

\* Corresponding author at: College of Chemical Engineering and Environment, China University of Petroleum, No. 18 Fuxue Road, Changping, Beijing 102249, China.

E-mail address: [baojian@cup.edu.cn](mailto:baojian@cup.edu.cn) (B. Shen).

<https://doi.org/10.1016/j.apcatb.2023.122822>

Received 21 February 2023; Received in revised form 25 April 2023; Accepted 27 April 2023

Available online 28 April 2023

0926-3373/© 2023 Elsevier B.V. All rights reserved.

conveniently with nano casting, and they applied their obtained Ni-containing SiC materials to dry reforming of methane. The conversions of methane and carbon dioxide on Ni/SiC-KIT-6 catalyst could reach 72.3% and 80% at 750 °C in DRM [23]. Park et.al prepared mesoporous SBA-15 coating Ni nanoparticles catalyst catalysts and the spatially confined NPs in the ordered mesopores were stable at high temperature reforming reaction. The most stable NP/SBA-15 showed the highest CH<sub>4</sub> and CO<sub>2</sub> conversion by almost approaching equilibrium conversions at 1073 K with the respective value of 91.4% and 93.1% with H<sub>2</sub>/CO ratio of 0.97, while the NP/SiO<sub>2</sub> showed the lowest values of 46.5% and 61.7% with H<sub>2</sub>/CO ratio of 0.72 [24].

The formation of metal alloys between nickel and other metals is also an important way to improve the carbon resistance of DRM catalysts. Tao et.al found Ni-Ce/TiO<sub>2</sub>-Al<sub>2</sub>O<sub>3</sub> catalysts showed high activity for CH<sub>4</sub> reforming. The conversions of methane and carbon dioxide on Ni-Ce/TiO<sub>2</sub>-Al<sub>2</sub>O<sub>3</sub> catalyst could reach 52.3% and 48.3% at 873 K and 96.8% and 97.9% at 1073 K [25]. Yusan and others researched a Co-Ni alloy that had been reduced, which explained its excellent performance [26]. Huang et.al found the Mo-promoted Ni catalysts had excellent catalytic performance [27]. Song et.al studied bimetallic NiFe/Al<sub>2</sub>O<sub>3</sub> promoted CH<sub>4</sub> and CO<sub>2</sub> conversion relative to monometallic Ni/Al<sub>2</sub>O<sub>3</sub> and the Ni<sub>3</sub>Fe alloy structure is favorable for the resistance of oxidation and coke deposition. CH<sub>4</sub> and CO<sub>2</sub> conversion on the NiFe/Al<sub>2</sub>O<sub>3</sub> was 26.6% and 37.8% with an H<sub>2</sub>/CO ratio of 0.67 at 823 K [28]. Similarly, Margossian demonstrated enhanced stability and high activity of bimetallic Ni-Fe nanoparticles compared to pure Ni-based catalysts [29]. Djaidja studied Ni-Fe bimetallic catalysts that had high catalytic activity and good carbon deposition resistance during long-time operation of high temperature DRM reaction. The conversions of methane and carbon dioxide were about 97%, with high yields of H<sub>2</sub> and CO (reaching 95% and 94% respectively) and a low amount of coke deposition [30]. It can be seen that the alloy and catalyst support play an important role in delaying carbon deposition in DRM.

Improving the activity of DRM and the ability of catalysts to resist carbon deposition have always been urgent problems to be solved. This work investigated the impact of Ni-Fe bimetallic synergy and incorporating C12A7-O<sup>2-</sup> in MCM-41 to reduce carbon deposition. Interestingly, we found that a small amount of H<sub>2</sub>O was produced by the reaction of methane and catalyst lattice oxygen in the early stage of the DRM reaction (TPSR-MS). Furthermore, the mechanism of reactive oxygen species formed by water adsorption and activation of CO<sub>2</sub> in DRM reaction and carbon deposition behavior was studied. In the methane reforming reaction, the main role of carbon dioxide is to eliminate carbon deposition (CO<sub>2</sub> + C = 2CO). The essence of catalyst carbon deposition was that the rate of carbon species produced by methane cracking was higher than carbon dioxide activation to eliminate carbon deposition. Therefore, an effective method to eliminate carbon deposition was to improve the adsorption and activation ability of the catalyst to CO<sub>2</sub>. Adding a tiny amount of water to the reforming process was the most straightforward and effective way to boost the adsorption of carbon dioxide by MC12A7 support. It provided theoretical guidance for further design and development of Ni-based DRM reaction catalysts with industrial potential.

## 2. Experimental

### 2.1. Catalyst preparation

For the preparation of mayenite (C12A7-O<sup>2-</sup>), weighing 37.86 g Al(NO<sub>3</sub>)<sub>3</sub>•9 H<sub>2</sub>O and 20.44 g Ca(NO<sub>3</sub>)<sub>2</sub>•4 H<sub>2</sub>O dissolved in 100 g water and stirring in a water bath at 353 K, then adding ammonia (25 wt%) to continue stirring for 3 h, then drying the gel for 10 h at 353 K, the dried sample was calcined in an air atmosphere at 1373 K for 10 h. Finally, the sample was ground and calcined for 6 h at 1623 K to obtain C12A7-O<sup>2-</sup> [31].

MCM-41 using market retail (Tianjin Nankai Catalyst Co., Ltd.), cation type H, all-silicon, 0.0008%Na<sub>2</sub>O, 95% crystallinity. C12A7-O<sup>2-</sup> and MCM-41 were extruded according to the mass ratio x and denoted as MC12A7-x (x = 1,2,4). The specific mass fraction of each component in the catalyst is shown in Table S1 of the support material.

The catalysts were prepared by co-impregnation of MCM-41 with aqueous Ni and Fe solutions using proper amounts of the nitrates precursors. 1.25 g nickel nitrate was dissolved in 5 g water and added dropwise to MCM-41. Then, the pre-cursor was dried at room temperature for 12 h, dried at 353 K for 2 h, and calcined at 823 K (4 K/min) for 4 h in an air atmosphere to obtain 5%Ni/MCM-41. Similarly, a series of 5%Ni-x%Fe/MCM-41 (x = 0.25,0.5,0.75,1,2 wt%) catalysts were prepared by impregnation on the support. Furthermore, Preparation of 5% Ni-0.50%Fe/MC12A7 catalysts using an aqueous solution of corresponding nitrates Ni(NO<sub>3</sub>)<sub>2</sub>•6 H<sub>2</sub>O (98%, Aladdin) and Fe(NO<sub>3</sub>)<sub>3</sub>•9 H<sub>2</sub>O (98.5%, Aladdin).

### 2.2. Catalysts characterization

The phase analysis of all catalysts was measured by Powder X-ray diffraction (Panalytical X'Pert Powder). A small amount of the sample to be tested was placed in a clean agate mortar and ground. After pressing in the mold, the appropriate test conditions were selected for testing. The test conditions were: voltage 40 kv, current 40 mA, Cu Kα X-ray source (λ = 1.5406 Å) radiation, angle 10–80°.

The specific surface area and mesoporous volume of all catalysts were obtained by low-temperature nitrogen physical adsorption experiments. Physical adsorption instrument model TriStar II 3020. Weigh a certain quality of the sample into the sample tube, the sample tube connected to the vacuum device at 623 K pretreatment for more than 8 h. The pretreated samples were installed in the measuring room for measurement. The specific surface area of the sample was calculated by the BET formula. The micropore-specific surface area and pore volume were obtained by the t-plot method. The total pore volume of the sample was obtained at a relative pressure of 0.99.

XPS was used to determine the oxygen vacancy concentration of the sample. The instrument model was Thermo Fisher K-Alpha, from the US. Determination method and procedure: The dry sample to be tested was pressed into the tablet and placed in the instrument for detection. If the sample was in the reduction state, the above operation should be carried out in the glove box. All the sample test results need to be calibrated by C1s peak (284.6 eV).

The morphology of samples was analyzed by SEM (Zeiss Gemini SEM 300). The accelerating voltages were 20–30 kV and 5–20 kV, respectively. The sample to be tested was fixed on a sample stand with conductive adhesive, and the sample stand was sprayed with gold under a vacuum to enhance the conductivity of the sample. Finally, the sample stand was transferred into a scanning electron microscope for observation.

The reduction degree of the active phase of all catalysts was characterized by H<sub>2</sub>-TPR. After crushing, 40–60 mesh sieving, and drying, the 100 mg sample was placed in a U-shaped quartz tube, and the sample was purged with carrier gas N<sub>2</sub> at a flow rate of 60 mL/min. At the same time, the sample was pretreated at a rate of 10 K/min to 773 K. The reduction mixture H<sub>2</sub>/Ar (10 vol% H<sub>2</sub>, 90 vol%Ar) was introduced into the reaction tube at a flow rate of 60 mL/min, and the temperature was increased to 1173 K at a rate of 10 K/min.

The reaction path of methane carbon dioxide reforming was characterized by Temperature Programmed Surface Reaction-Mass Spectrometry (TPSR-MS). The experiments were performed in fix-bed reactors and the compositions of the reactor outlet were measured by online mass spectrometry (Hiden, QGA Quantitative Gas Analysis Mass Spectrometer).

The <sup>13</sup>CH<sub>4</sub> (Sigma-Aldrich, 99 atom% <sup>13</sup>C) isotope labeling experiment is used to track the methane reaction path. We carried out the

reaction on a fixed bed device, filled the catalyst with 1 g, and detected the exhaust gas online by mass spectrometry. A programmed temperature system controlled the fixed bed. After setting the reaction temperature and heating rate, the catalyst was first reduced in the  $H_2$  atmosphere for 2 h, purged in switching  $N_2$  for 1 h, and then introduced into  $^{13}CH_4$ . After the reaction, the exhaust gas was introduced into the British Hiden QGA quantitative gas analyzer mass spectrometer.

The  $D_2O$  (Sigma-Aldrich, 99.9 atom% D) isotope labeling experiment is used to track the water reaction path. The experimental operation is the same as the  $^{13}CH_4$  isotope labeling experiment. After the reaction, the exhaust gas was introduced into the British Hiden QGA quantitative gas analyzer mass spectrometer.

The carbon deposition of all catalysts was analyzed by thermogravimetric analysis (TG). The samples were placed in a weighing system with a certain heating program to determine the weight change of the samples with temperature. Instrument model: Germany NETZSCH-STA 409 PC. DSC stability range: 20–1500 K, sensitivity: 4–4.5  $\mu V/mW$ . TG Thermal Balance Accuracy: 0.1  $\mu g$ .

### 2.3. Catalytic activity test

In order to test the activity of the catalyst, the reactor system operating at constant pressure was used as described in this work. The catalyst is placed in the middle of the reactor, the rest of the space is filled with quartz sand, and a Gas Chromatography system (Agilent 8890) is used to analyze the gas composition of the reaction gas mixture after passing through the reactor every 25 min to monitor the catalytic activity. The TCD detector is used to detect hydrogen and methane, and the valve-switching system is used. There are three chromatographic columns, 2 feet Porapak Q, 80 ~ 100 mesh, 6 feet Porapak Q 80 ~ 100 mesh, 8 feet Molecular sieve, 60 ~ 80 mesh, and the carrier gas is argon. Second, FID uses a dual detector using central cutting technology. The first column HP-innowax detects methanol and C6–C10 aromatics separate components below C5 and blows to the second column alumina column to analyze C1–C5 alkanes. The carrier gas is nitrogen. The initial temperature of the column box was 323 K maintained for 2 min, and then increased to 453 K at a rate of 10 K / min for 30 min

For DRM reaction evaluation, the catalyst was placed in the middle of the reactor, while the gas distribution in the inlet was kept uniform. Previously to the DMR tests, the catalyst is treated with hydrogen (20 mL/min, 973 K, 2 h) and then the hydrogen on the catalyst surface is purged with pure nitrogen. After the reduction was completed, the reaction temperature set to 1073 K, and the mixture of methane and carbon dioxide ( $CH_4 = 25$  mL/min,  $CO_2 = 25$  mL/min) was introduced into the reactor. Finally, the gas product entered the GC and MS for online detection.

The  $CH_4$  and  $CO_2$  conversions, and  $H_2/CO$  ratio were calculated by the following equations:

$$X_{CH_4} = \frac{F_{CH_4}^{in} - F_{CH_4}^{out}}{F_{CH_4}^{in}} \quad (1)$$

$$X_{CO_2} = \frac{F_{CO_2}^{in} - F_{CO_2}^{out}}{F_{CO_2}^{in}} \quad (2)$$

$$H_2/CO = \frac{F_{H_2}^{out}}{F_{CO}^{out}} \quad (3)$$

where  $F_i^{in}$  was the flow rate of each component (i) in the inlet feed, and  $F_i^{out}$  was the flow rate of each component (i) in the outlet feed,  $X_i$  are the conversion [32].

## 3. Results and discussion

### 3.1. Structure and textural properties of the catalysts

The XRD patterns of 5%Ni-x%Fe/MCM-41 ( $x = 0, 0.25, 0.5, 0.75, 1, 2$ ) catalysts are displayed in Fig. S1 (refer to support material). Low-angle XRD patterns of the samples (Fig. S1a) showed Bragg peaks which are characteristic of MCM-41 structure. The all catalysts peak at the  $2\theta$  value of  $2.42^\circ, 4.14^\circ, 4.80^\circ$ , which corresponds to  $d(100)$  and  $d(110)$  and  $d(200)$  in MCM-41. The position of the Bragg peak changes slightly, depending on the concentration of Fe. With the increase of Fe content, the structure of MCM-41 was slightly distorted. The XRD patterns showed that all catalysts have a broad reflection at around  $23^\circ$ , which was attributed to amorphous silica in MCM-41 support in Fig.S1(b) [33]. The characteristic peaks of NiO were observed at  $37.2^\circ, 43.2^\circ$ , and  $62.8^\circ$  in all catalysts. FeOx was not detected due to low Fe content. With the increase of FeOx loading, the reflection width of NiO changes slightly, indicating that the cell size changes. There is a strong interaction between NiO and  $SiO_2$  or FeO, which forms a solid solution with NiO and  $SiO_2$ . Other authors have proved it [34,35].

The X-ray diffraction (XRD) patterns of Ni-Fe/MC12A7 catalysts were shown in Fig.S2 (refer to support material). All samples exhibited similar diffraction peaks, especially the support component (mayenite,  $C12A7-O^{2-}$ ) phase, and indicated that the calcium aluminate has been introduced into MCM-41. As shown in Fig.S2(b). The characteristic peaks of  $C12A7-O^{2-}$  were observed at  $8.1^\circ, 23.4^\circ, 27.8^\circ, 29.7^\circ, 33.4^\circ, 36.7^\circ, 41.2^\circ, 46.6^\circ, 55.2^\circ, 57.4^\circ$  and agrees well with mayenite (PDF#70–2144). With the increase of the mass fraction of mayenite in the support, the peak at the  $2\theta$  value of  $2.42^\circ$  decreases (Fig.S2a), and the diffraction peak intensity of mayenite increases.

The XRD patterns of reduced catalysts were shown in Fig.S3 and Fig. S4 (refer to support material). The diffraction peak of reduced catalysts at  $51.3^\circ$ , which should be attributed to the formation of  $Ni_3Fe$  alloy by some Ni and Fe. The formation of  $Ni_3Fe$  alloy could change the interaction between Ni and carrier to a certain extent. This was consistent with the  $H_2$ -TPR characterization study results. Fe has excellent redox ability, which transforms the DRM reaction pathway into a Mars-van Krevelen mechanism. Previous work have reported that Ni-Fe exhibits a dealloying and realloying process, making rapid removal of carbon deposition [29,53]. Due to the limitation of analytical instruments, we currently have no information about the dealloying and realloying process in the present catalyst system.

The XRD patterns of the spent catalysts and comparison with the fresh catalysts were shown in Fig.S5 and Fig.S6 (refer to support material). As shown in Fig.S5, the characteristic peaks of carbon were observed at  $26.3^\circ$ , for Ni-Fe/MCM-41 spent catalysts, which shows that graphite carbon deposition appeared on the catalyst during the DRM. The XRD patterns showed that Ni-Fe/MCM-41 catalysts have a broad reflection at around  $23^\circ$ , which indicates that MCM-41 maintains a stable structure at reaction temperature. The diffraction peak intensity of carbon deposition on Ni-Fe/MCM-41 catalyst is lower than that on Ni/MCM-41 catalyst, which may be attributed to the appearance of  $Ni_3Fe$  alloy during the DRM process, which enhances the interaction between metal and support, and the formation of  $Ni_3Fe$  alloy improves the resistance of coke deposition. It can be seen from the figure that as the Fe loading increases, the  $Ni_3Fe$  alloy grains on the spent catalyst become larger, resulting in a decrease in catalytic activity. As shown in Fig.S6, the characteristic peaks of mayenite were observed in spent Ni-Fe/MC12A7 catalysts, which shows that the crystal structure of mayenite was stable during the DRM. At the same time, the characteristic peaks of carbon were also observed at  $26.3^\circ$ .

The nitrogen adsorption-desorption (Fig. S7) of MCM-41 and Ni-Fe/MCM-41 show type IV isotherm and mesoporous features. Due to the capillary condensation of  $N_2$ , it increases sharply in a narrow range of relative pressure ( $P/P_0 = 0.25-0.4$ ), indicating uniform mesopores[36]. The support provided the expected maximum surface area. After Ni

**Table 1**

Texture data of catalysts prepared by using MCM-41 as support.

Sample	$S_{\text{BET}}$ ( $\text{m}^2\text{g}^{-1}$ ) <sup>a</sup>	$V_{\text{total}}$ ( $\text{cm}^3\text{g}^{-1}$ ) <sup>b</sup>	$D_p$ (nm) <sup>c</sup>
MCM-41	1264	1.140	3.1
5%Ni /MCM-41	1074	0.952	3.1
5%Ni-0.25%Fe/MCM-41	1101	0.979	3.1
5%Ni-0.5%Fe/MCM-41	1037	0.884	3.0
5%Ni-0.75%Fe/MCM-41	1009	0.879	3.0
5%Ni-1%Fe/MCM-41	930	0.799	3.0
5%Ni-2%Fe/MCM-41	933	0.784	3.0

<sup>a</sup> Specific surface area calculated by BET model method<sup>b</sup> The total pore volume was calculated by adsorbed amounts at P/Po = 0.99<sup>c</sup> average pore diameter area calculated by Barrett-Joyner-Halenda model method (adsorption curve)**Table 2**

Texture data of catalysts prepared by using MC12A7 as support.

Sample	$S_{\text{BET}}$ ( $\text{m}^2\text{g}^{-1}$ ) <sup>a</sup>	$V_{\text{total}}$ ( $\text{cm}^3\text{g}^{-1}$ ) <sup>b</sup>	$D_p$ (nm) <sup>c</sup>
5%Ni-0.5%/MC12A7-1	654	0.569	3.0
5%Ni-0.5%/MC12A7-2	664	0.559	3.0
5%Ni-0.5%/MC12A7-4	761	0.660	3.0

<sup>a</sup> Specific surface area calculated by BET model method<sup>b</sup> The total pore volume was calculated by adsorbed amounts at P/Po = 0.99<sup>c</sup> average pore diameter area calculated by Barrett-Joyner-Halenda model method (adsorption curve)

addition and catalyst calcination, the specific surface area decreased due to partial blockage of the pores. Further increasing the Fe loading, the specific surface area decreased. The pore size was not affected by the addition of Ni or Fe, which was about 3 nm. This indicated that the decrease in surface area was due to pore blockage. The change of the specific surface area of catalyst was also related to the interaction between metal and support.

The structural parameters of the catalyst are listed in Table 1 and Table 2. From the BET specific surface area analysis results, all catalysts showed mesoporous structure. However, the BET surface area and pore volume of the catalyst decreased significantly with the increase of the mass fraction of mayenite in the support. This indicates that the specific surface area of mayenite is relatively low compared to MCM-41. The catalysts display type IV isotherms with a hysteresis loop of the H1-type, according to the IUPAC classification (Fig.S8). The pore size of the catalyst is concentrated at 3 nm.

### 3.2. The effect of metal–support Interaction

The H<sub>2</sub>-TPR profiles of the as-prepared catalysts with different supports in 5%Ni-xFe/MCM-41 (x = 0, 0.25, 0.5, 0.75, 1, 2) catalysts were shown in Fig. 1. The H<sub>2</sub>-TPR distribution of the samples was divided into two temperature regions: region I (500–600 K) and region II (700–900 K). Regions I and II should be related to the reduction of supported metal oxide species in different interactions on the support surface. It is well known that the interaction between nickel oxide and the support can affect the reduction temperature. Nickel species can be more readily reduced at lower temperatures when the interaction is weak. For 5%Ni/MCM-41 catalysts, it exhibited a weak reduction peak at low temperatures (below 600 K) due to the reduction of a small amount of large NiO particles present on the surface of the support [37]. The reduction peak of small nickel oxide particles was mainly concentrated between 723 and 823 K [38–41]. Owing to introducing the second metal Fe, the reduction temperature of the bimetallic MCM-41 catalyst will change. Although the reduction of a small amount of doped Fe species cannot be excluded, the main peak was temporarily attributed to the reduction of Ni<sup>2+</sup> in the silica structure. It can be seen that the intensity of the first peak (region I) shifts to high temperature with

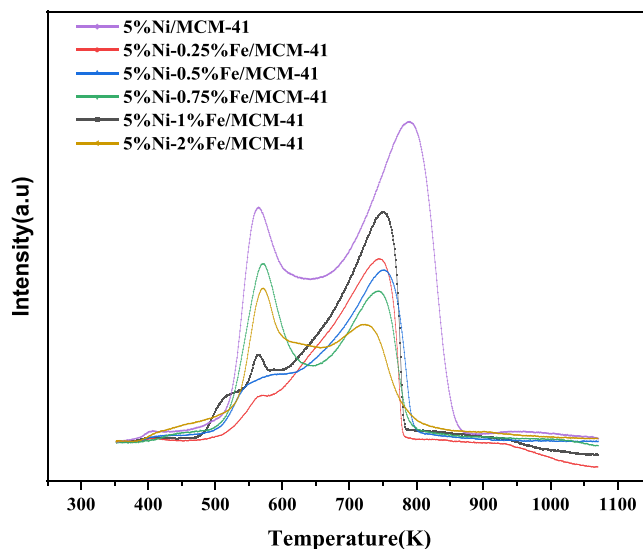


Fig. 1. H<sub>2</sub>-TPR profiles of 5%Ni-xFe/MCM-41 (x = 0, 0.25, 0.5, 0.75, 1, 2) catalysts.

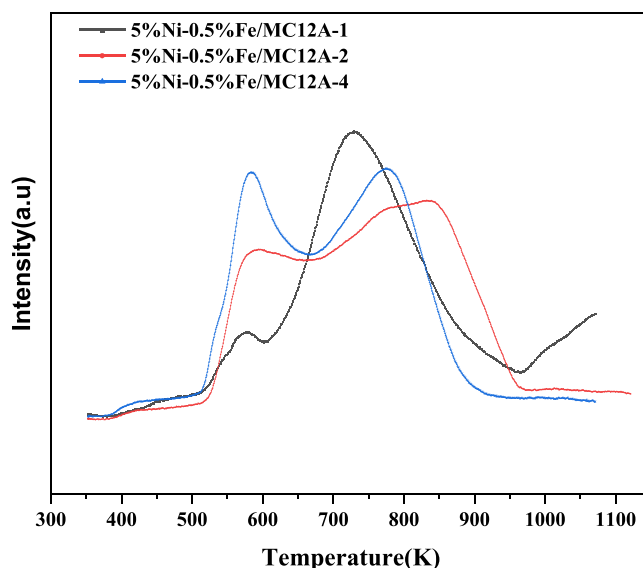


Fig. 2. H<sub>2</sub>-TPR profiles of 5%Ni-0.5%Fe/MC12A7 catalysts.

introducing Fe, indicating that the addition of Fe enhances the interaction between NiO particles and the support. The peak of hydrogen consumption in region II of all samples was attributed to the reduction of highly dispersed Ni<sup>2+</sup> species, which interact strongly with the support and form a nickel silicate monolayer on the surface of the MCM-41 substrate [42].

The H<sub>2</sub>-TPR profiles of the as-prepared catalysts with Ni-Fe/MC12A7 contents are shown in Fig. 2. The content of mayenite in the support affected the interaction between Ni and the support. With the increase of the proportion of mayenite in the support, the reduction temperature of Regions I (<600 K) decreases.

### 3.3. Catalyst oxygen vacancy characterization

The surface chemical composition of the catalyst was studied by XPS analysis. Fig. 3 showed the high-resolution XPS spectra of Ni 2p<sub>3/2</sub>, Fe 2p<sub>3/2</sub>, and O 1s. As shown in Fig. 3(a), the typical Ni<sup>2+</sup> spectrum of the prepared sample shows a primary signal at 855–856 eV, and its satellite peak shows at 861–862 eV [43]. This indicates that the Ni species



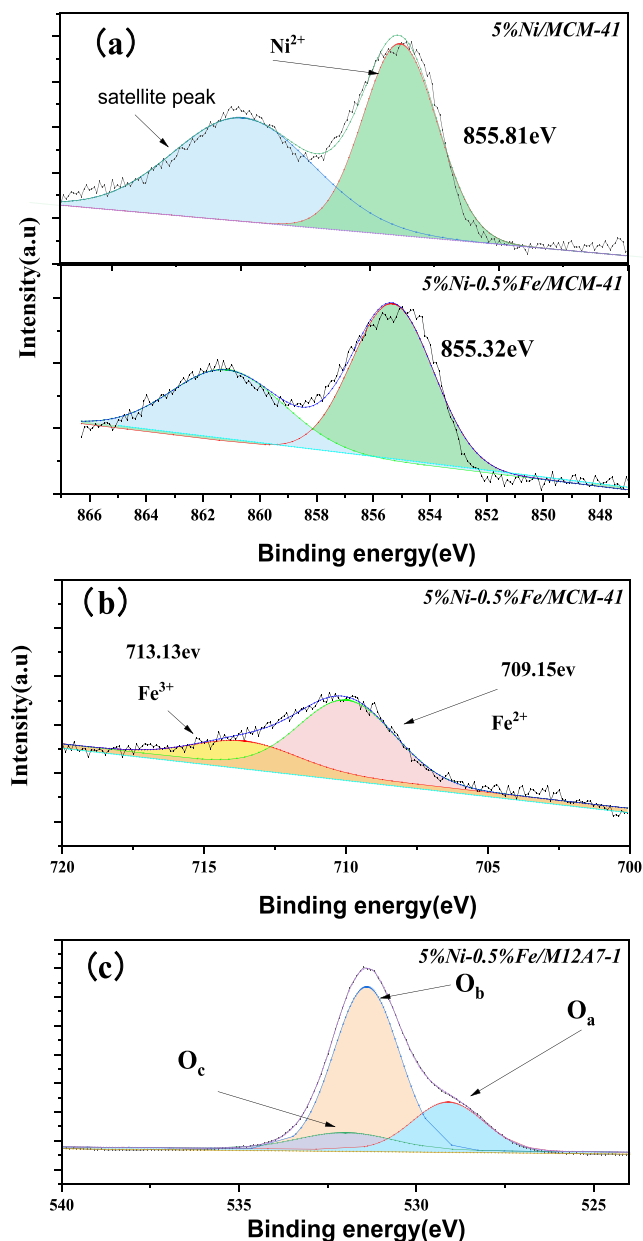


Fig. 3. XPS profile of 5%Ni/MCM-41, 5%Ni-0.5%Fe/MCM-41, 5%Ni-0.5%Fe/MC12A7-1 catalysts: (a) Ni 2p<sub>3/2</sub> spectra (b) Fe 2p<sub>3/2</sub> spectra (c) O 1s spectra.

mainly exist in the state of Ni<sup>2+</sup>, which is consistent with the results of XRD analysis. In general, Ni 2p<sub>3/2</sub> is higher than the reference pure NiO (853.8 ~ 854.5 eV), indicating the transfer of Ni electrons and the interaction between Ni<sup>2+</sup> and the support. The addition of Fe reduces the interaction between the Ni species and the mayenite support, which can be observed in the H<sub>2</sub>-TPR pattern.

Fig. 3(b) is the Fe 2p<sub>3/2</sub> spectrum. With Fe 2p<sub>3/2</sub>, the binding energy strongly depends on the state of Fe. The peak can be decomposed into two peaks of 709.15 eV and 713.13 eV, which belong to Fe<sup>2+</sup> and Fe<sup>3+</sup>, respectively [44]. After calcination of the catalyst, the Fe element exists in an oxidized state. In addition, there is no obvious satellite peak in the spectrum.

The O 1s spectrum is shown in Fig. 3(c), showing three different oxygen species. Three overlapping peaks were observed in the O 1s region, which was located at 529.5, 531.0 eV, and 532.0 eV, respectively, belonging to lattice oxygen, surface adsorbed oxygen, and adsorbed water species [45]. Due to the structural symmetry caused by

the change of the Fe-O bond, Fe inevitably increases the original electron cloud density around the O 1s orbital [46]. In DRM, surface adsorbed oxygen plays an important role due to its redox function. The surface chemisorbed oxygen is the most active oxygen in the reaction process due to its higher mobility. In addition, due to Fe metal, the overall lattice oxygen content also increased.

### 3.4. Catalyst activity evaluation

The DRM catalytic performance of 5%Ni-xFe/MCM-41 (x = 0, 0.25, 0.5, 0.75, 1, 2) catalysts was investigated at 1073 K (Fig. 4). To illustrate the synergy effect of Fe addition on catalyst activity, the reaction was carried out continuously for more than 300 min under atmospheric pressure. Compared with the reference sample without Fe, the activity of the catalyst with Fe loading less than 1.00 wt% was significantly improved. When the Fe loading is 0.50 wt%, the methane conversion rate was the highest, which was 83%. The conversion of these samples remains constant for over 300 min. In general, the optimum loading of Fe is 0.50 wt%, and the methane conversion rate begins to decrease when the loading exceeds 1 wt%.

It can be seen from the above that Fe as an active promoter can further improve the activity of nickel-based catalysts in DRM. However, the catalyst is prone to carbon deposition with the reaction time. To prolong the life of the catalyst, introducing mayenite modified MCM-41 was used as support. Therefore, a series of Ni-Fe/MC12A7 catalysts for DRM reaction were prepared to systematically explore their activity and stability.

The effect of mayenite on the DRM catalytic performance of Ni-Fe/MCM-41 was investigated. The experimental results were shown in Fig. 5. Compared with Ni-Fe/MCM-41 catalyst, the Ni-Fe/MC12A7-4 (mass ratio of MCM-41 to mayenite 4) improved the activity of DRM. When mayenite is further increased, the excessive C12A7-O<sup>2-</sup> content in the catalyst will inhibit the activity of the catalyst, because the specific surface area of the catalyst decreased. We further evaluate the stability of the catalyst, a long-term DRM test was conducted for about 1800 min, using the prepared Ni-Fe/MC12A7-1 catalyst (refer to support material Fig.S9). It can be seen that the activity of 5% Ni-0.5%Fe / MC12A7-1 catalyst remained stable within 1800 min, then the conversion of methane and carbon dioxide began to decrease, and the reactor pressure increased, which indicated that the catalyst carbon deposition began to deactivate seriously.

In addition, when using 5%Ni-0.5%Fe/MCM-41 catalyst, the reaction tube was blocked when the DRM reaction lasted for 800 min. Through previous experiments, it was found that Ni-loaded catalysts had carbon deposition due to severe methane cracking reaction. The carbon deposition will be transformed into filamentous carbon and graphite carbon with increasing reaction time. Filamentous carbon cannot deactivate the catalyst immediately, but it will block the reaction tube when it accumulates to a certain extent. This will not lead to a significant decrease in catalytic activity but will cause the reactor to hold pressure.

The effect of catalyst morphology was obtained by SEM test (Fig. S10). Fig.S10 (a) and Fig.S10 (b) are fresh 5%Ni-0.5%Fe/MCM-41 and C12A7-O<sup>2-</sup> catalyst morphology, Fig.S10 (c) can be seen on the catalyst both MCM-41 and mayenite morphology. The catalyst appeared on filamentous carbon morphology over the spent of 5%Ni/MCM-41 catalyst. However, filamentous carbon can also be observed on 5%Ni-0.5%Fe/MC12A7-4, but the length of filamentous carbon was smaller than that of the catalyst.

Fig. 6 showed the results of thermogravimetric analysis (TG) of the spent catalyst after continuous reaction at 1073 K for 1200 min. It was observed that there was less carbon deposition in the MC12A7 catalyst. The highest amount of carbon deposition was given on the 5%Ni-0.5%Fe/MCM-41 catalyst. With the increase of mayenite in the support, the carbon deposition of the catalyst gradually decreased, which indicates that the mayenite had a significant improvement effect on delaying the carbon deposition of the catalyst. The reason is that the microporous

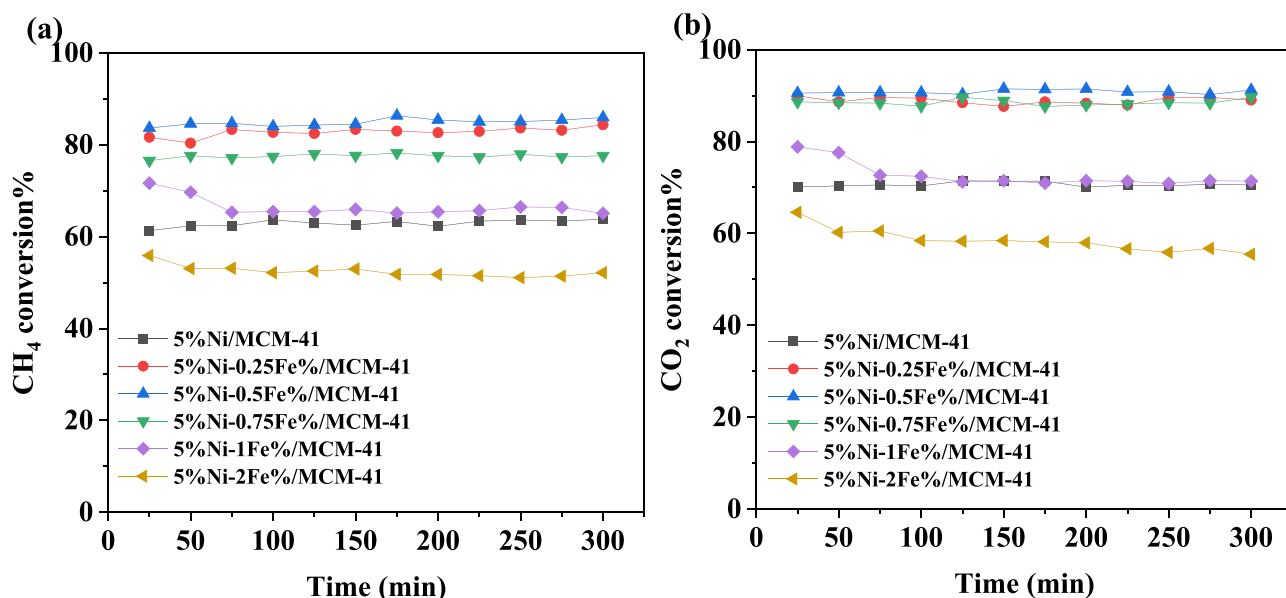


Fig. 4. DRM catalytic performance over 5%Ni-xFe/MCM-41 ( $x = 0, 0.25, 0.5, 0.75, 1, 2$ ) catalysts (Condition:  $\text{CO}_2/\text{CH}_4 = 1:1$ ,  $P = 1$  atm,  $T = 1073$  K,  $\text{GHSV} = 6000 \text{ mL} \cdot \text{g}_{\text{cat}}^{-1} \cdot \text{h}^{-1}$ ).

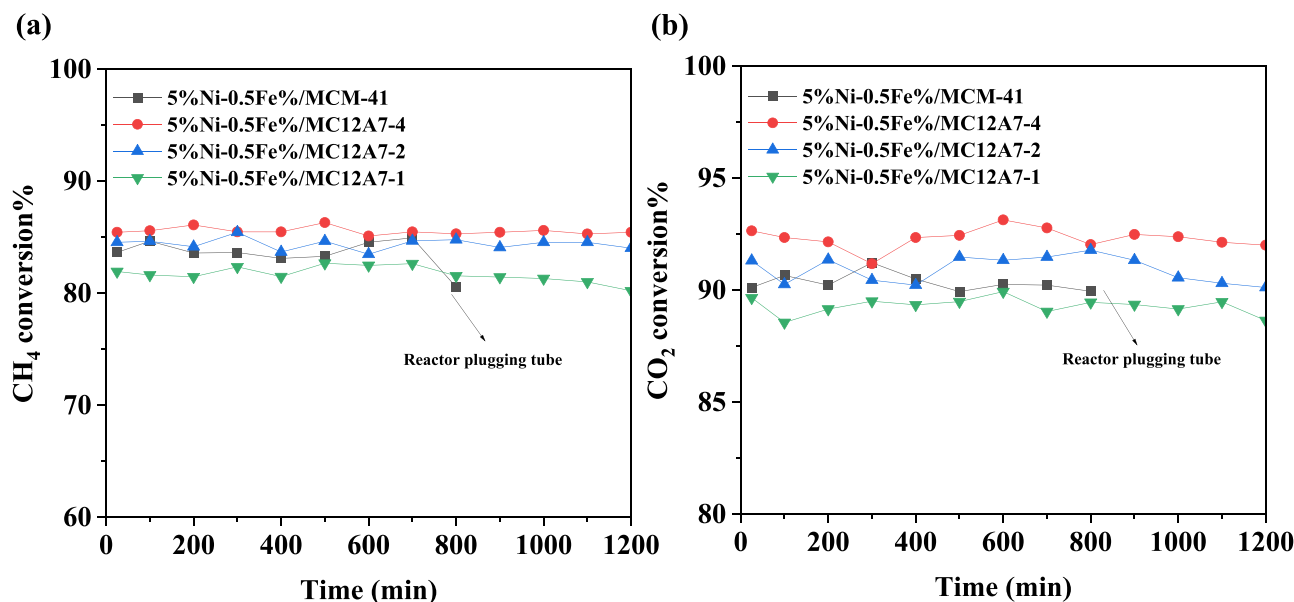


Fig. 5. DRM catalytic performance over 5%Ni-0.5Fe/MCM-41 and 5%Ni-0.5Fe/MC12A7 catalysts (Condition:  $\text{CO}_2/\text{CH}_4 = 1:1$ ,  $P = 1$  atm,  $T = 1073$  K,  $\text{GHSV} = 6000 \text{ mL} \cdot \text{g}_{\text{cat}}^{-1} \cdot \text{h}^{-1}$ ).

crystals of C12A7 had a cubic structure with two molecules per unit cell. It was characterized by a positively charged lattice framework  $[\text{Ca}_{24}\text{Al}_{28}\text{O}_{64}]^{4+}$ , including 12 subnanometer-sized cages with a free space diameter of about 0.4 nm. The remaining two  $\text{O}^{2-}$  ions are encapsulated in the cage [47]. The free oxygen ions in the mayenite can migrate to the MCM-41 on the support and further react with the carbon deposition to form carbon monoxide.

### 3.5. The effect of catalyst lattice oxygen on reaction

In order to study the effect of lattice oxygen on the reaction. The activation mechanism of CH<sub>4</sub> and CO<sub>2</sub> on Ni-Fe/MCM-41 and Ni-Fe/MC12A7-4 was studied by temperature programmed mass spectrometry (TPSR-MS). As shown in Fig. 7(a), CH<sub>4</sub> and CO<sub>2</sub> decreased slightly, but H<sub>2</sub> and CO did not change significantly in regin 2. However, the H<sub>2</sub>O

signal appears to be upside down. H<sub>2</sub>O may be involved in the reforming reaction as an inducing intermediate. Olsbye et al. considered that H<sub>2</sub>O and OH generated in the reforming reaction are very important active groups and play a decisive role in the subsequent reforming reaction [48]. In the temperature region, 3, CH<sub>4</sub>, CO<sub>2</sub>, and H<sub>2</sub>O all decreased significantly, and H<sub>2</sub> and CO began to form, which was mainly the reforming reaction process.

As shown in Fig. 7(b), the variation of product signals on different catalysts is significantly different. In temperature region 2, the reaction begins with the decrease of CH<sub>4</sub>, H<sub>2</sub>O, and CO<sub>2</sub> increased immediately to a certain extent, H<sub>2</sub> increased after some time, and CO did not change significantly. In temperature region 3, H<sub>2</sub>O begins to decrease, and CO and H<sub>2</sub> increased significantly, which should be that the lattice oxygen in the catalyst took part in the reaction to generate CO and H<sub>2</sub>. XPS proves that the catalyst has lattice oxygen. In temperature region 4, H<sub>2</sub>O

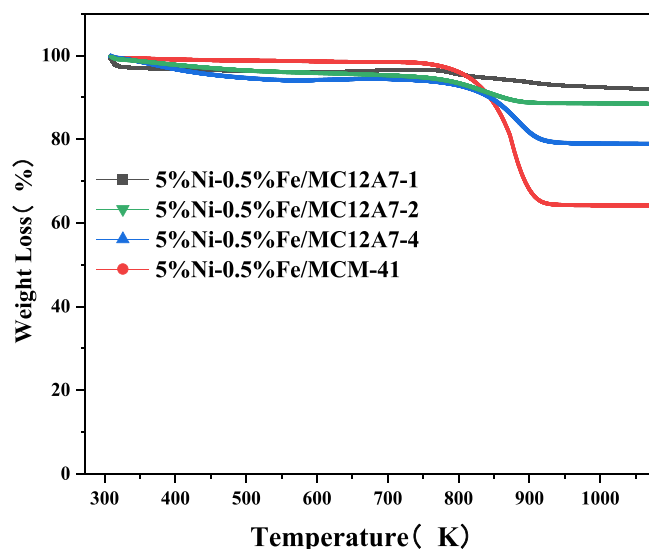


Fig. 6. TGA patterns for 5%Ni-0.5%Fe/MC12A7 and 5%Ni-0.5%Fe/MCM-41 spent catalysts for DRM reaction. Condition:  $\text{CO}_2/\text{CH}_4 = 1:1$ ,  $P = 1$  atm,  $T = 1073$  K,  $\text{GHSV} = 6000 \text{ mL}_{\text{cat}}^{-1} \cdot \text{h}^{-1}$ .

increased significantly again, accompanied by a slight increase in  $\text{CO}_2$ ,  $\text{H}_2$ , and  $\text{CO}$  decreased to a certain extent, which may be like the reaction on 5%Ni-0.5%Fe/MCM-41. Before the start of the reforming reaction, a certain amount of  $\text{H}_2\text{O}$  was generated, but it decreased rapidly, where  $\text{H}_2\text{O}$  may play an induction role. Compared with 5%Ni-0.5%Fe/MCM-41, 5%Ni-0.5%Fe/MC12A7-4 due to the existence of lattice oxygen, it has a lower starting point at the reaction temperature. The early reaction process is mainly the reaction of  $\text{CH}_4$  and lattice oxygen to produce  $\text{H}_2\text{O}$  and  $\text{CO}_2$ . When the temperature rises to a higher temperature, the main products of the reaction on the two catalysts are  $\text{H}_2$  and  $\text{CO}$ . The  $\text{H}_2\text{O}$  generated during the reaction may be induced.

### 3.6. The role of $\text{H}_2\text{O}$ in the conversion of $\text{CO}_2$ and $\text{CH}_4$

To more clearly study the effect of the catalyst on the reaction and the role of water in the methane reforming process,  $^{13}\text{CH}_4$  was used to track the reaction path. Under the reaction conditions ( $\text{GHSV} = 6000 \text{ mL}_{\text{cat}}^{-1} \cdot \text{h}^{-1}$ ,  $P = 1$  atm,  $T = 1073$  K), a stream of  $^{13}\text{CH}_4$  was introduced into the continuous flow of  $\text{CO}_2$  atmosphere, and the mass spectrometry response curves of each product are shown in Fig. 8 (a). The appearance of  $^{13}\text{CO}$  indicated that  $^{13}\text{C}$  in  $^{13}\text{CH}_4$  enters  $^{13}\text{CO}$ . Methane was first adsorbed and dissociated into  $^{13}\text{CH}_x$  and  $\text{H}_2$  in Ni catalyst, and  $^{13}\text{CH}_x$  is further oxidized (the catalyst provides free oxygen ions) into  $^{13}\text{CO}$ . The formation of  $^{12}\text{CO}$  was due to the adsorption of  $\text{CO}_2$  on the support during the reaction, and Ni provides  $\text{CO}_2$  active sites. Therefore,  $\text{CH}_4$  and  $\text{CO}_2$  were adsorbed on the metal nickel and the support, respectively, and were activated and dissociated at the interface between the nickel and the support to produce  $\text{CO}$  and  $\text{H}_2$ . After the gas of  $^{13}\text{CH}_4$  was introduced,  $\text{H}_2$  and  $^{13}\text{CO}$  are produced at the same time. This indicated that methane dissociation and  $\text{CH}_x$  oxidation were rapid reactions. When the  $^{13}\text{CH}_4$  decreases,  $^{13}\text{CO}_2$  continues to be produced. This is because free oxygen ions over MC12A7 oxidizes  $^{13}\text{CH}_x\text{O}$  to  $^{13}\text{CO}_2$ .

Fig. 8(b) showed the change of mass spectrum signal of each product when  $^{13}\text{CH}_4$  enters  $\text{CO}_2$  over 5%Ni/MCM-41. The reaction paths are different over the two types of catalysts. After the disappearance of  $^{13}\text{CH}_4$ ,  $^{13}\text{CO}_2$  is almost reduced to zero over the 5%Ni/MCM-41 catalyst. This indicated that there is little active oxygen on the surface of the 5% Ni/MCM-41 catalyst, which is not enough to oxidize  $^{13}\text{CH}_x$  from  $^{13}\text{CH}_4$  decomposition. The signals of  $\text{H}_2$ ,  $^{12}\text{CO}$ , and  $^{13}\text{CO}$  products over 5%Ni/MCM-41 catalyst are less than those on 5%Ni/MC12A7.

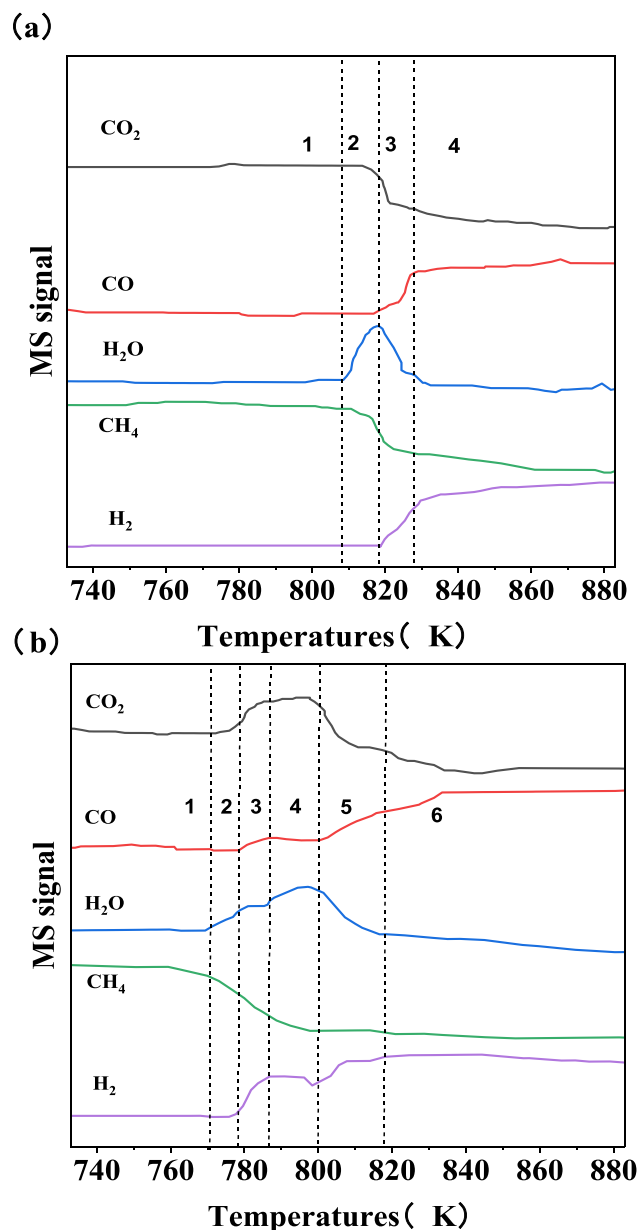
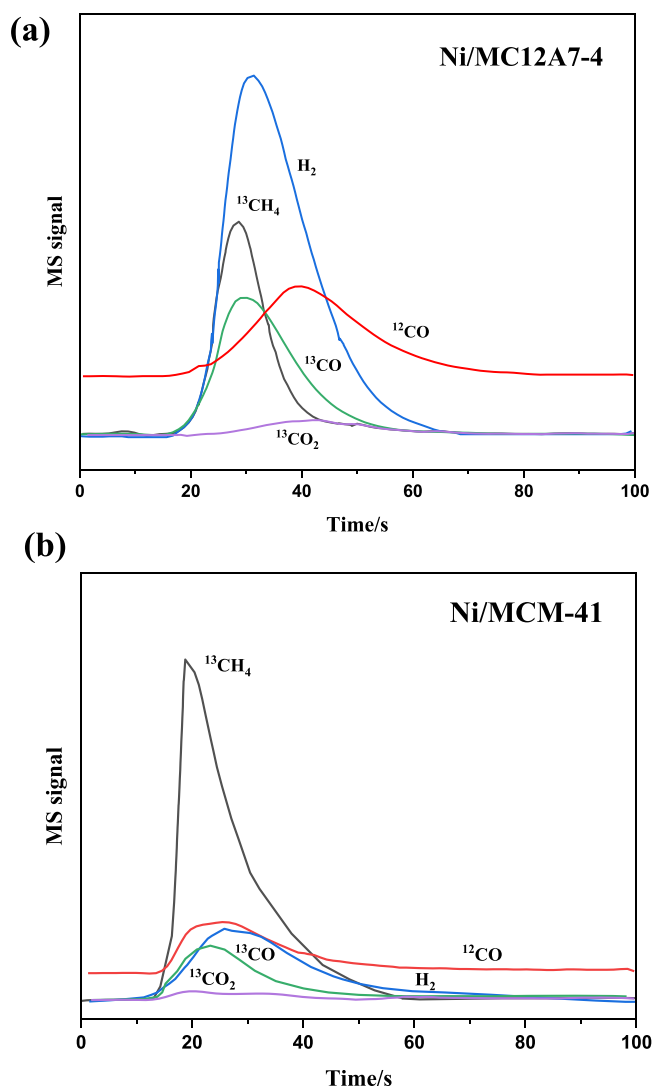


Fig. 7. The ion signal change rule in TPSR-MS: (a) 5%Ni-0.5%Fe/MCM-41 (b) 5%Ni-0.5%Fe/MC12A7-4.

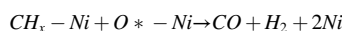
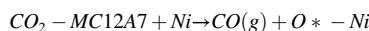
To understand the effect of carbon dioxide on the surface active material of the catalyst, the stream of carbon dioxide was introduced into the continuous methane flow system. The signal response curve of each product was shown in Fig. 9.  $\text{CO}$  was produced immediately after  $\text{CO}_2$  enters the system, and the appearance of  $\text{H}_2$  lags  $\text{CO}$ .  $\text{CO}_2$  dissociates into  $\text{CO}$  and reactive oxygen species on the catalyst surface. The reaction is fast, followed by the dissociation of  $\text{CH}_4$ , and the oxidation of  $\text{CH}_x$  to produce  $\text{CO}$  and  $\text{H}_2$ . Similar results were obtained on Ni/MCM-41 catalyst. However, the signals of  $\text{CO}$  and  $\text{H}_2$  are much smaller than Ni/MC12A7-4 catalyst. The reason is that the adsorption of  $\text{CO}_2$  on MCM-41 support is weaker than that of MC12A7, which hinders the further reaction of  $\text{CO}_2$  and  $\text{CH}_x$ . Kell studied the effect of water on  $\text{CO}_2$  adsorption. Water may promote or impede  $\text{CO}_2$  adsorption, enhance or decrease the rate of  $\text{CO}_2$  uptake, or even affect the structural integrity of the adsorbent according to different materials [49]. We explored the effect of water on the MC12A7 catalyst system in methane reforming reaction. Fig. 10 exhibited that a stream of  $\text{H}_2\text{O}$  was introduced in  $\text{CH}_4$  and  $\text{CO}_2$  atmosphere under reaction condition



**Fig. 8.** Mass spectrum response curve of each product upon a stream of  $^{13}\text{CH}_4$  was introduced in carbon dioxide atmosphere and the: (a) 5%Ni/MC12A7-4, (b) 5%Ni/MCM-41.

( $\text{CH}_4/\text{CO}_2/\text{H}_2\text{O}=10/10/1$ ,  $P = 1 \text{ atm}$ ,  $T = 1073 \text{ K}$ ). When water appears, the  $\text{CO}_2$  signal decreases and CO appears immediately, which indicates that water accelerates the adsorption of  $\text{CO}_2$  on the catalyst surface and the dissociation of  $\text{CO}_2$  into CO. The  $\text{H}_2$  signal appears later than CO, indicating that the oxidation reaction of  $\text{CH}_x$  and free oxygen ions occur after the dissociation of  $\text{CO}_2$ .

DFT calculations showed that  $\text{CO}_2$  adsorption on  $\text{Ca}_{12}\text{Al}_{14}\text{O}_{33}$  is facilitated by the presence of water, suggesting an Eley-Rideal type mechanism in which  $\text{H}_2\text{O}$  preferentially adsorbs on the  $\text{Ca}_{12}\text{Al}_{14}\text{O}_{33}$  surface and activates adjacent O atoms, which are more reactive with  $\text{CO}_2$  compared to water-free  $\text{Ca}_{12}\text{Al}_{14}\text{O}_{33}$  surfaces [50]. This indicated that the following reactions occur on the catalyst:



Therefore, we speculated that the presence of  $\text{H}_2\text{O}$  in the early stage of the methane reforming reaction enhances the adsorption of  $\text{CO}_2$  on the MC12A7 catalyst and activates the oxygen ion to further react with  $\text{CH}_x$  to produce a large amount of CO and  $\text{H}_2$ .

The effect of water content on the adsorption and activation of  $\text{CO}_2$ , the changes of  $\text{CO}_2$  and water after  $\text{CO}_2$  and water passing through fresh catalyst at different ratios were studied by MS (in Fig. 11). Under reaction conditions ( $T = 1073 \text{ K}$ ,  $P = 0.1 \text{ Mpa}$ ,  $\text{WHSV} = 6000 \text{ mL} \cdot \text{gcat}^{-1} \cdot \text{h}^{-1}$ ), all products were normalized with argon as internal standard. When the content of water in the feed increases, it can be seen that the carbon dioxide signal reduces, indicating that  $\text{CO}_2$  adsorption is enhanced by  $\text{H}_2\text{O}$  adsorption. DFT calculation showed that water coverage increases and  $\text{CO}_2$  adsorption energy decreases [51]. The  $\text{H}_2\text{O}$  can be regarded as the active material, ensuring that  $\text{CO}_2$  adsorption is promoted. It can be categorised as an E-R mechanism [50,51]. In addition, the  $m/z = 1$  signal height and  $m/z = 2$  with increasing water in the feed, indicate that the role of  $\text{H}_2\text{O}$  also promotes methane decomposition ( $\text{CH}_4 = \text{CH}_x + \text{H}$ ). Because the adjacent O atom is activated after  $\text{H}_2\text{O}$  adsorption, reaction with  $\text{CH}_x$  produces CO and  $\text{H}_2$  ( $\text{CH}_x + \text{O}^* = \text{CO} + \text{H}_2$ ). The continuous consumption of  $\text{CH}_x$  drives the forward methane decomposition.

Considering the simplification of the reaction steps, the study of the effect of water on the catalytic reaction is based on Ni-based catalysts. The presence of Fe can also promote the reaction. We also discussed the effect of the amount of water on the activity of the Ni-Fe catalytic system (Fig. 12). It can be seen that water can promote the conversion of methane and carbon dioxide. This is consistent with the conclusion of online mass spectrometry analysis of the effect of  $\text{H}_2\text{O}$  inflow on methane carbon dioxide reforming reaction over Ni/M12A7-4 catalyst.

Amadeo et al. studied the competitive relationship between methane and water on Ni active sites in methane steam reforming reaction by DFT calculation and kinetic measurements experiments. DFT calculations show that when CHO and OH species adsorb on top of Ni atom and on a three-fold site, respectively. The adsorption sites of methane and water are different. The kinetic experimental indicate that competition between  $\text{H}_2\text{O}$  and  $\text{CH}_4$  intermediate species should not be expected at low  $\text{H}_2\text{O}/\text{CH}_4$  ratios. Thus, in this condition methane conversion would be related directly to the  $\text{H}_2\text{O}/\text{CH}_4$  ratio. When the water in the feed increases, methane is more easily converted. In our work, the online mass spectrometry analysis of the effect of  $\text{H}_2\text{O}$  inflow on methane carbon dioxide reforming reaction over Ni/M12A7-4 catalyst under reaction conditions in Fig. 11. When the water in the feed increases, the  $\text{CH}_4$  signal decreases significantly. Besides, after adding water to the methane reforming reaction, the methane conversion rate increased from 85.5% to 94.65% in Fig. 12. This shows that water promotes the conversion of methane. Previous analysis showed that most of the CO in the product comes from the  $\text{CH}_x$  oxidation step, so  $\text{H}_2\text{O}$  promotes the reaction with  $\text{CH}_x$  for  $\text{H}_2$  and CO. When the molar amount of feed water is one-tenth of methane, it can improve the conversion of methane. The competition between methane and water at Ni active sites is not intense. Only when the water content is high, competitive adsorption will be formed, resulting in a decrease in methane conversion.

In the absence of carbon dioxide, the product distribution of methane and water feed on the catalyst was analyzed by online mass spectrometry (reference support material Fig S11-S13). It can be seen that the carbon monoxide signal increases with the increase in water content. However, methane is not mostly converted in the methane and water feed reforming reaction system, and the methane signal is high with carbon monoxide by MS. The amount of syngas produced is less than methane carbon dioxide and water feed (reference support material Fig S14). The mechanism of water in accelerating methane carbon dioxide reforming differs from that of methane wet reforming.

As shown in Fig. 13, we performed isotope  $\text{D}_2\text{O}$  labelling experiments to study the effect of water on the reaction. When Ar and  $\text{D}_2\text{O}$  were used as feeds, the signal intensity of DH ( $m/z = 3$ ) was difficult to observe. When  $\text{CH}_4 + \text{D}_2\text{O} + \text{CO}_2$  were used as feeds, the DH ( $m/z = 3$ ) signal appeared, indicating that  $\text{D}_2\text{O}$  reacts with  $\text{CH}_x$  to form DH. Besides, after adding water to the methane reforming reaction, the methane conversion rate increased from 85.5% to 94.65% in Fig. 12. This shows that water promotes the conversion of methane. When  $\text{D}_2\text{O}$  and  $\text{CH}_4$  were



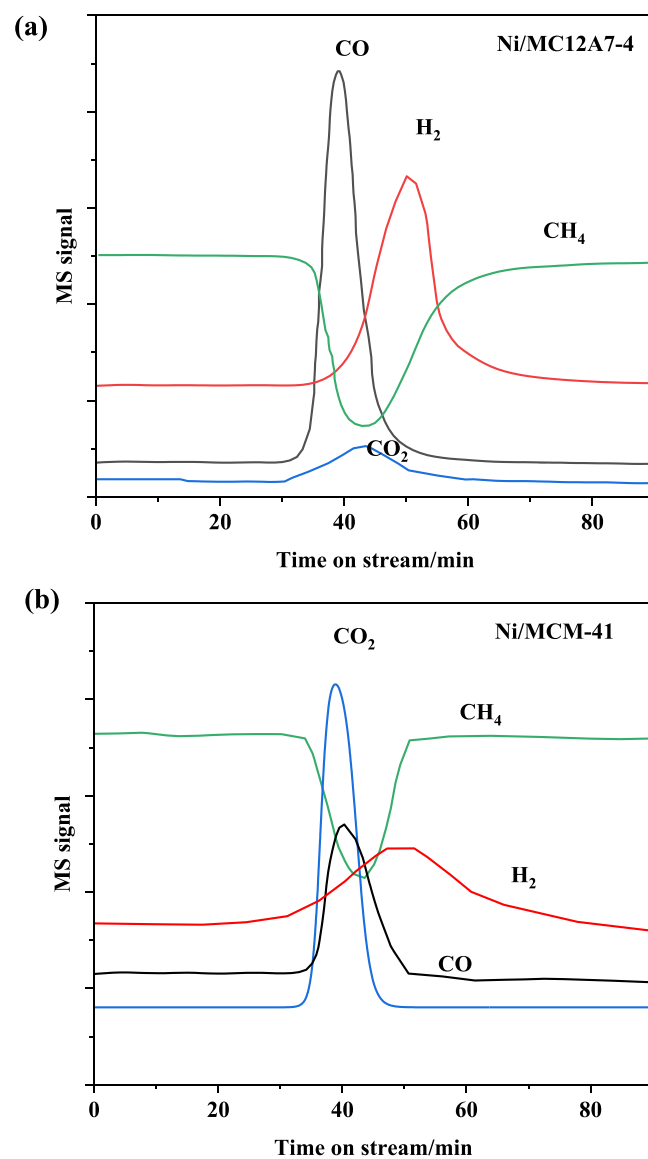


**Fig. 9.** The mass spectrum response curve of each product upon a stream of CO<sub>2</sub> was introduced in methane atmosphere: (a) 5%Ni/MC12A7-4, (b) 5%Ni/MCM-41.

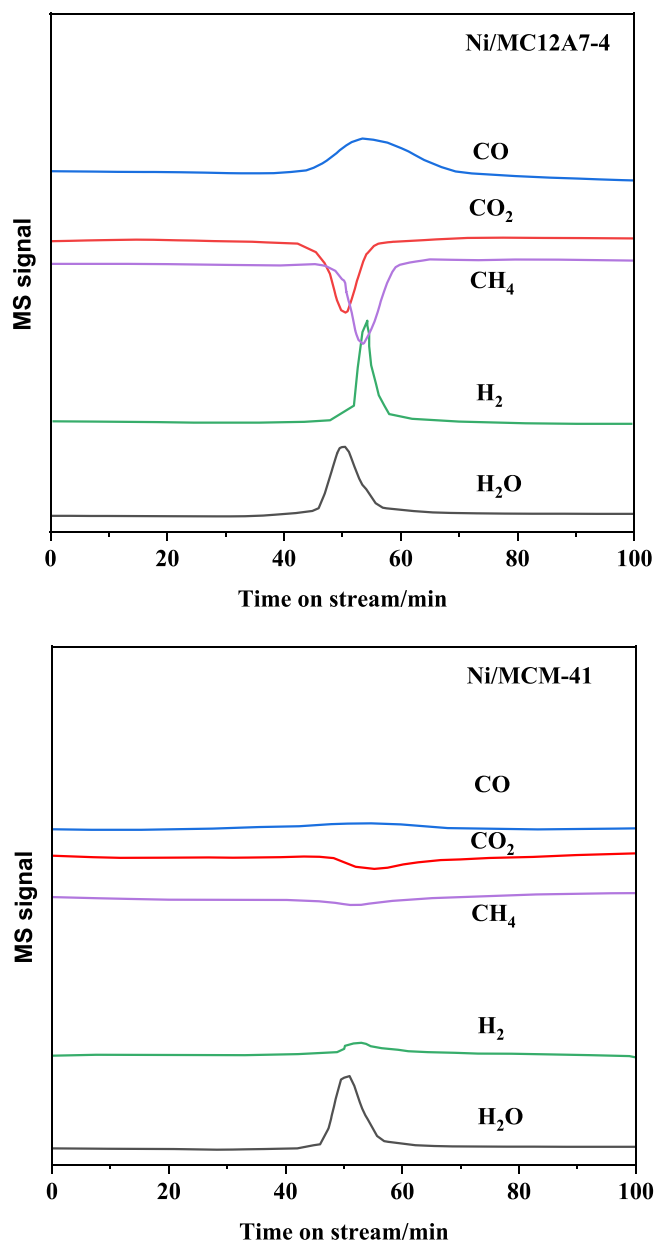


Fig. 10. The mass spectrum response curve of each product upon a stream of  $\text{H}_2\text{O}$  was introduced in  $\text{CH}_4$  and  $\text{CO}_2$  atmosphere: (a) 5%Ni/MC12A7-4, (b) 5% Ni/MCM-41.

used as feeds, we can see that the CO ( $m/z = 28$ ) and hydrogen ( $m/z = 2$ ) signals in the product have decreased. This is due to the competitive adsorption of water and methane. The  $\text{CO}_2$  ( $m/z = 44$ ) signal occurs because of the Water-Gas Shift Reaction. Therefore, adding a small amount of water in the  $\text{CH}_4$ - $\text{CO}_2$  dry reforming reaction process can significantly accelerate the methane cracking reaction. The source of hydrogen in the product is not only from methane cracking, but also from the reaction of  $\text{CH}_x$  and  $\text{H}_2\text{O}$  to produce  $\text{H}_2$  and CO.

### 3.7. The role of $\text{H}_2\text{O}$ in the removal of carbon deposition

Carbon deposition is an important problem hindering the industrialisation of DRM. The effect of water in the feed on the carbon deposition of the catalyst is also worth studying. As shown in Fig. 14, the amount of carbon formed during the DRM process was quantified by thermogravimetric (TG) analysis of the spent 5%Ni-0.5%Fe/MC12A7-4 catalysts after 20 h continuous DRM reaction at 1073 K. According to

previous studies[52], the carbon deposited on the surface of nickel-based catalysts can be divided into three types: amorphous carbon  $\text{C}_\alpha$ , filamentous carbon  $\text{C}_\beta$ , and graphite carbon  $\text{C}_\gamma$ . It has been reported that the deposited  $\text{C}_\alpha$  is an active carbon species during the DRM process, which can be easily eliminated by oxidation or  $\text{H}_2$  reduction at 523–623 K with thermal desorption of  $\text{H}_2\text{O}$  and  $\text{CO}_2$ . Compared with carbon dioxide reforming of methane, the catalyst did not lose weight in the presence of water at 523–623 K (Fig. 13). This implies that  $\text{H}_2\text{O}$  consumes  $\text{C}_\alpha$  on the catalyst in time during the reaction. In addition,  $\text{C}_\beta$  has relatively high activity and can be eliminated at relatively low temperatures. In contrast to  $\text{C}_\alpha$  and  $\text{C}_\beta$ ,  $\text{C}_\gamma$  needs a high temperature (more than 873 K) to be removed by oxidation. The presence of  $\text{H}_2\text{O}$  delays the carbon deposition of the catalyst. It was found that  $\text{H}_2\text{O}$  could reduce the surface coverage of  $\text{C}^*$  in DRM, indicating inhibition of carbon deposition. There are ways to eliminate carbon deposition in water as follows:

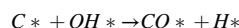
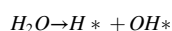


Fig. 11 also shows that  $\text{H}_2\text{O}$  is conducive to the emergence of  $\text{H}^*$ . The dissociation reactions of  $\text{H}_2\text{O}$  would inhibit  $\text{C}^*$  generation, which was consistent with the previous analysis. However, there is no water in the reaction system, the main reaction of carbon deposition removal is  $\text{C}^* + \text{O}^* \rightarrow \text{CO}^*$ . Therefore, the other role of water was to change the major path of  $\text{C}^*$  conversion, as water proved abundant  $\text{OH}^*$  and  $\text{H}^*$ .

## 4. Conclusions

In this study, the Ni-Fe/MC12A7 catalyst was designed and prepared to improve the catalytic activity and stability for reforming methane and  $\text{CO}_2$ . The MC12A7 support, which was prepared by introducing  $\text{C12A7-O}^{2-}$  in MCM-41, has a larger specific surface area and pore volume, and there are free oxygen ions, which can migrate on the support and react with carbon deposition to form carbon monoxide, inhibiting carbon deposition. In DRM, the surface chemisorbed oxygen is the most active oxygen in the reaction process due to its higher mobility. Active oxygen plays a key role in the oxidation of  $\text{CH}_x$ , which is produced by the dissociation of methane. The isotope  $^{13}\text{CH}_4$  tracing experiment showed the appearance of  $^{13}\text{CO}$  indicating that the product CO mainly comes from the  $\text{CH}_x$  oxidation reaction and a small amount of  $^{12}\text{CO}$  comes from the dissociation of  $\text{CO}_2$ , exhibiting the interaction of  $\text{CH}_4$  and  $\text{CO}_2$  with active species on the catalyst. The  $^{13}\text{CO}$  signal is greater than  $^{12}\text{CO}$ , identifying that most of the CO come from the  $\text{CH}_x$  oxidation step.

In addition, due to Fe metal, the overall lattice oxygen content also increased (XPS proved). XPS and temperature programmed mass spectrometry (TPSR-MS) studies indicated that the existence of lattice oxygen in Ni-Fe/MC12A7 catalysts facilitate a lower starting point at the reaction temperature and a certain amount of  $\text{H}_2\text{O}$  was generated from the reaction of  $\text{CH}_4$  with lattice oxygen in the initial stage of the reforming reaction.

Considering the induction of  $\text{H}_2\text{O}$ , we further explored the effect of  $\text{H}_2\text{O}$  on the MC12A7 catalyst system in methane reforming reaction using online mass spectrometry. When a small amount of water enters the reforming reaction system can accelerate the adsorption of  $\text{CO}_2$  on the MC12A7 support and promote methane dissociation, the  $\text{H}_2$  signal appears later than CO, indicating the oxidation reaction of  $\text{CH}_x$  occurs after the dissociation of  $\text{CO}_2$ . The isotope  $\text{D}_2\text{O}$  tracing experiment showed the DH ( $m/z = 3$ ) signal appeared, indicating that  $\text{D}_2\text{O}$  reacts with  $\text{CH}_x$  to form DH. From the perspective of chemical equilibrium, the continuous consumption of  $\text{CH}_x$  forces the methane cracking to move forward, so the role of water is to accelerate methane conversion. The presence of  $\text{H}_2\text{O}$  is conducive to the emergence of  $\text{H}^*$ . The dissociation

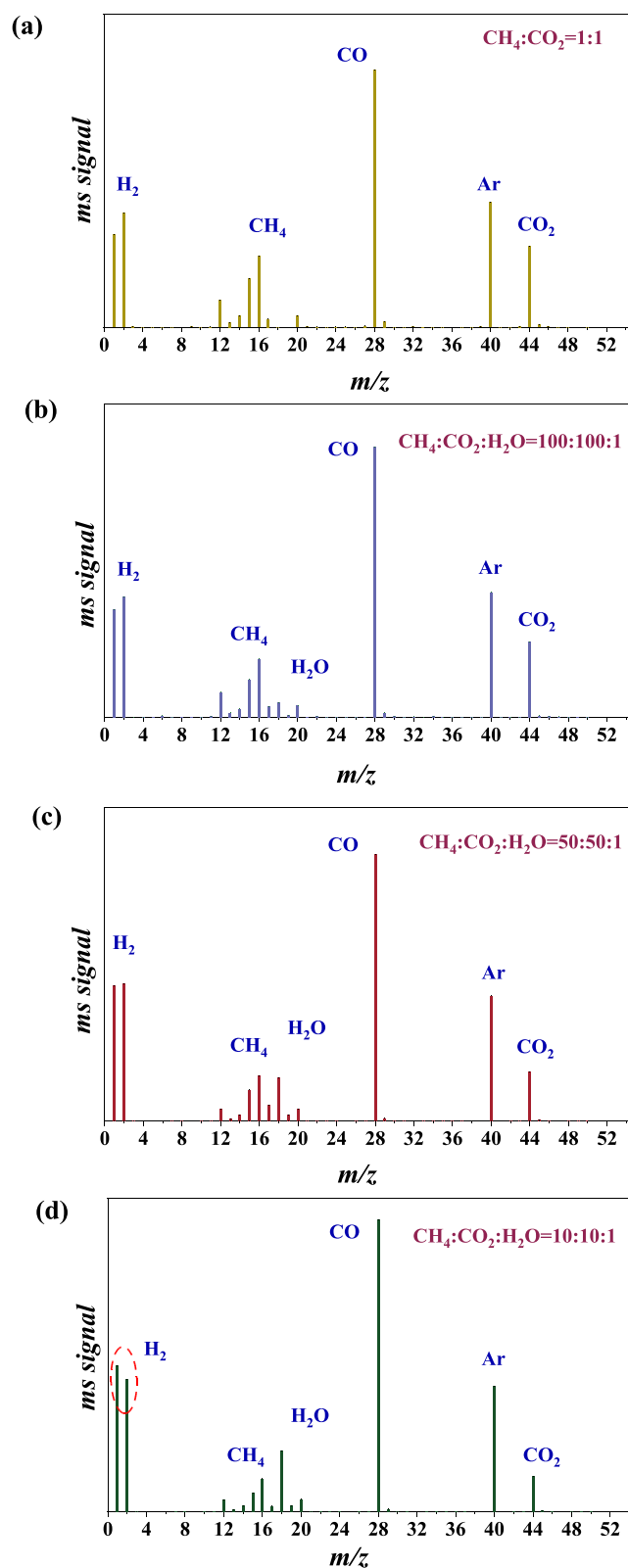


**Fig. 11.** Online mass spectrometry analysis of the effect of H<sub>2</sub>O inflow on methane carbon dioxide reforming reaction over Ni/M12A7-4 catalyst under reaction conditions. (a)  $\text{CH}_4:\text{CO}_2=1$  (b)  $\text{CH}_4:\text{CO}_2:\text{H}_2\text{O}=100:100:1$  (c)  $\text{CH}_4:\text{CO}_2:\text{H}_2\text{O}=50:50:1$  (d)  $\text{CH}_4:\text{CO}_2:\text{H}_2\text{O}=10:10:1$ . ( $T=1073\text{ K}$ ,  $P=0.1\text{ Mpa}$ ,  $\text{WHSV}=6000\text{ mL}\cdot\text{g}_{\text{cat}}^{-1}\cdot\text{h}^{-1}$ , Ar as internal standard gas,  $\text{CO}_2/\text{Ar}=2$ ).

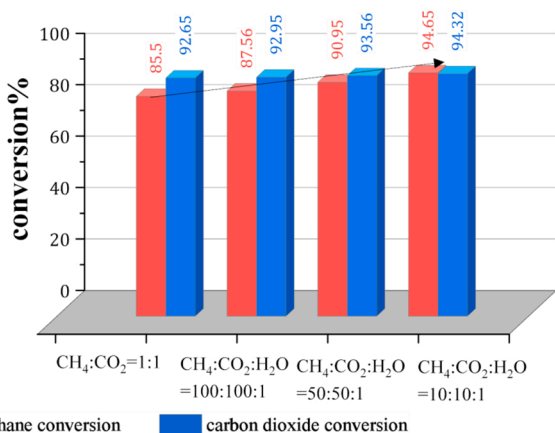


Fig. 12. The effect of different water inflow on methane reforming reaction over 5%Ni-0.5%Fe/MC12A7-4 catalyst. (T = 1073 K, P = 0.1Mpa, WHSV=6000 mL·g<sub>cat</sub><sup>-1</sup>·h<sup>-1</sup>, TOS=2 h).

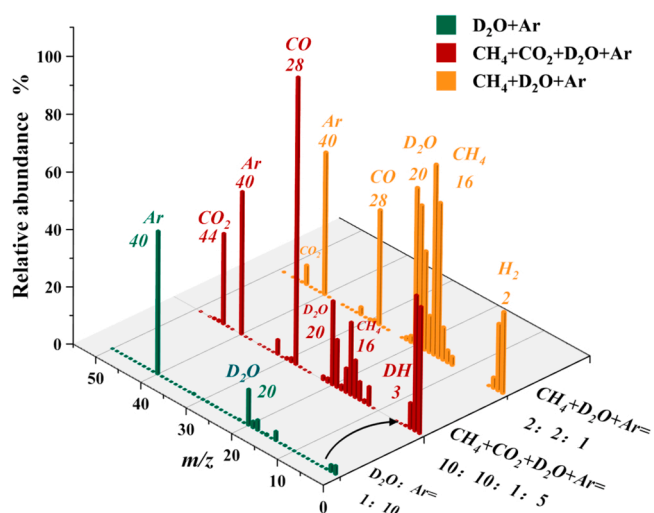


Fig. 13. Online analysis of reaction product with mass spectrum by using D<sub>2</sub>O+Ar, CH<sub>4</sub>+CO<sub>2</sub>+D<sub>2</sub>O+Ar, CH<sub>4</sub>+D<sub>2</sub>O+Ar as the feed respectively. Reaction conditions: T = 1073 K, P = 0.1Mpa, WHSV = 6000 mL·g<sub>cat</sub><sup>-1</sup>·h<sup>-1</sup>, Ni/MA12A7-4 catalyst.

reactions of H<sub>2</sub>O would inhibit C\* generation (C\*+H\*=CH\*, C\*+OH\*=CO\*+H\*), and H<sub>2</sub>O consumes Cα on the catalyst in time during the reaction. However, there is no water in the reaction system, the main reaction of carbon deposition removal is C\*+O\*→CO\*. Therefore, the other role of water was to change the major path of C\* conversion, as water proved abundant OH\* and H\*.

#### CRediT authorship contribution statement

**Lingxiang Huang**: Conceptualization, Catalyst design & preparation, Evaluation and Characterization, Writing. **Yue Ma**: Evaluation and Characterization. **Mufan Niu**: Evaluation. **Shenyong Ren**: Characterization. **Qiaoxia Guo**: Characterization and Discussion. **Chunming Xu**: Reviewing and Discussion. **Baojian Shen**: Conceptualization, Catalyst design, Writing, Supervision.

#### Declaration of Competing Interest

The authors declare that they have no known competing financial interests or personal relationships that could have appeared to influence the work reported in this paper.

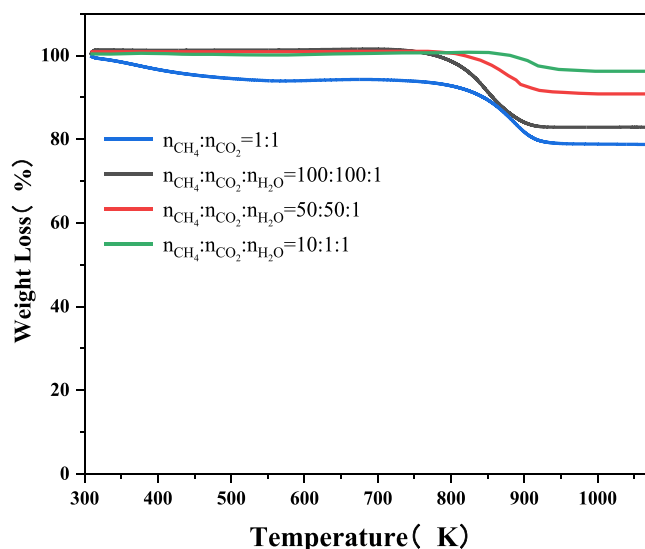


Fig. 14. TGA patterns for 5%Ni-0.5%Fe/MC12A7-4 catalysts at different water contents in DRM.

#### Data Availability

Data will be made available on request.

#### Acknowledgements

The authors acknowledge the financial support provided for this project by the Foundation for the Innovative Research Groups of the National Natural Science Foundation of China (22021004).

#### Appendix A. Supporting information

Supplementary data associated with this article can be found in the online version at [doi:10.1016/j.apcatb.2023.122822](https://doi.org/10.1016/j.apcatb.2023.122822).

#### References

- [1] M.D. Burkart, N. Hazari, C. Tway, E.L. Zeitler, Opportunities and challenges for catalysis in carbon dioxide utilization, *ACS Catal.* 9 (2019) 7937–7956, <https://doi.org/10.1021/acscatal.9b02113>.
- [2] W. Chu, L.N. Wang, P.A. Chernavskii, A.Y. Khodakov, Glow-discharge plasma-assisted design of cobalt catalysts for Fischer–Tropsch synthesis, *Angew. Chem. Int. Ed.* 47 (2008) 5052–5055, <https://doi.org/10.1002/ange.200800657>.
- [3] L. Spadaro, F. Arena, M.L. Granados, M. Ojeda, F. Frusteri, Metal-support interactions and reactivity of Co/CeO<sub>2</sub> catalysts in the Fischer–Tropsch synthesis reaction, *J. Catal.* 234 (2005) 451–462, <https://doi.org/10.1016/j.jcat.2005.07.006>.
- [4] O. Kwon, R. Huang, T. Cao, J.M. Vohs, R.J. Gorte, Dry reforming of methane over Ni supported on LaMnO<sub>3</sub> thin films, *Catal. Today* 382 (2021) 142–147, <https://doi.org/10.1016/j.cattod.2021.08.001>.
- [5] Q. Wang, W. Wang, M. Cao, S. Li, P. Wang, J. He, R. Li, X.L. Yan, Effect of interstitial carbon atoms in core-shell Ni<sub>3</sub>ZnCo<sub>0.7</sub>/Al<sub>2</sub>O<sub>3</sub> catalyst for high-performance dry reforming of methane, *Appl. Catal. B: Environ.* 317 (2022), 121806, <https://doi.org/10.1016/j.apcatb.2022.121806>.
- [6] J.A. Mendoza-Nieto, J.S. Tehuacanero-Cuapa, J. Arenas-Alatorre, H. Pfeiffer, Nickel-doped sodium zirconate catalysts for carbon dioxide storage and hydrogen production through dry methane reforming process, *Appl. Catal., B* 224 (2018) 80–87, <https://doi.org/10.1016/j.apcatb.2017.10.050>.
- [7] A. Di Giuliano, F. Giancaterino, C. Courson, Development of a Ni–CaO–mayerite combined sorbent-catalyst material for multicycle sorption enhanced steam methane reforming, *Fuel* 234 (2018) 687–699, <https://doi.org/10.1016/j.fuel.2018.07.071>.
- [8] J.L. Rogers, M.C. Mangarella, A.D. D'Amico, J.R. Gallagher, M.R. Dutzer, E. Stavitski, J.T. Miller, C. Sievers, Differences in the nature of active sites for methane dry reforming and methane steam reforming over nickel aluminate catalysts, *ACS Catal.* 6 (2016) 5873–5886, <https://doi.org/10.1021/acscatal.6b01133>.
- [9] S. Ali, M.M. Khader, M.J. Almarri, Ni-based nano-catalysts for the dry reforming of methane, *Today* 343 (2020) 26–37, <https://doi.org/10.1016/j.cattod.2019.04.066>.



- [10] K. Mette, S. Kühl, A. Tarasov, M.G. Willinger, J. Kröhnert, S. Wrabetz, A. Trunschke, M. Scherzer, F. Girsig, H. Düdder, K. Kähler, K.F. Ortega, M. Muhler, R. Schlögl, M. Behrens, T. Lunkenbein, High-temperature stable Ni nanoparticles for the dry reforming of methane, *ACS Catal.* 6 (2016) 7238–7248, <https://doi.org/10.1021/acscatal.6b01683>.
- [11] A. Luengnaruemitchai, A. Kaengsilalai, Activity of different zeolite-supported Ni catalysts for methane reforming with carbon dioxide, *Chem. Eng. J.* 114 (2008) 96–102, <https://doi.org/10.1016/j.cej.2008.05.023>.
- [12] Z.Z. Qin, J. Chen, X.L. Xie, X. Luo, T.M. Su, H.B. Ji, CO<sub>2</sub> reforming of CH<sub>4</sub> to syngas over nickel-based catalysts, *Environ. Chem. Lett.* 18 (2020) 997–1017, <https://doi.org/10.1007/s10311-020-00996-w>.
- [13] J. Li, J. Li, Q.S. Zhu, Carbon deposition and catalytic deactivation during CO<sub>2</sub> reforming of CH<sub>4</sub> over Co/MgO catalyst, *Chin. J. Chem. Eng.* 26 (2018) 2344–2350, <https://doi.org/10.1016/j.cjche.2018.05.025>.
- [14] L. Zhang, X. Wang, X.F. Shang, M.W. Tan, W.Z. Ding, X.G. Lu, Carbon dioxide reforming of methane over mesoporous nickel aluminate/ $\gamma$ -alumina composites, *J. Energy Chem.* 26 (2017) 93–100, <https://doi.org/10.1016/j.jechem.2016.08.001>.
- [15] J. Yang, X. Lu, C. Han, H. Liu, D. Dong, L. Mo, Q.H. Wei, H.C. Tao, S. Cui, L. H. Wang, Glycine-assisted preparation of highly dispersed Ni/SiO<sub>2</sub> catalyst for low-temperature dry reforming of methane, *Int. J. Hydrog. Energy* 47 (2022) 32071–32080, <https://doi.org/10.1016/j.ijhydene.2022.07.104>.
- [16] Y.D. Song, E. Ozdemir, S. Ramesh, A. Adishev, S. Subramanian, A. Harale, M. Albuli, B.A. Fadhel, A. Jamal, D. Moon, S.H. Choi, C.T. Yavuz, Dry reforming of methane by stable Ni–Mo nanocatalysts on single-crystalline MgO, *Science* 367 (2020) 777–781, <https://doi.org/10.1126/science.aav2412>.
- [17] N. Abdullah, N. Ainirazali, H. Ellapan, Structural effect of Ni/SBA-15 by Zr promoter for H<sub>2</sub> production via methane dry reforming, *Int. J. Hydrog. Energy* 46 (2021) 24806–24813, <https://doi.org/10.1016/j.ijhydene.2020.07.060>.
- [18] R.F. Peng, Y.M. Chen, B.X. Zhang, Z.P. Li, X. Cui, C.W. Guo, Y.C. Zhao, J.Y. Zhang, Tailoring the stability of Ni-Fe/mayenite in methane-carbon dioxide reforming, *Fuel* 284 (2021), 118909, <https://doi.org/10.1016/j.fuel.2020.118909>.
- [19] S.W. Yang, J.N. Kondo, K. Hayashi, M. Hirano, K. Domen, H. Hosono, Partial oxidation of methane to syngas over promoted C12A7, *Appl. Catal., A* 277 (2014) 239–246, <https://doi.org/10.1016/j.apcata.2004.09.030>.
- [20] E. Savuto, D. Carlo A, K. Gallucci, S. Natali, E. Bocci, Characterization and performance analysis of an innovative Ni/Mayenite catalyst for the steam reforming of raw syngas, *Fuel* 194 (2017) 348–356, <https://doi.org/10.1016/j.fuel.2017.01.022>.
- [21] M.B. Bahari, C.R. Mamat, A.A. Jalil, N.S. Hassan, W. Nabgan, H.D. Setiabudi, N. Dai-Viet, B.T. Phuong Thuy, Mesoporous alumina: a comprehensive review on synthesis strategies, structure, and applications as support for enhanced H<sub>2</sub> generation via CO<sub>2</sub>-CH<sub>4</sub> reforming, *Int. J. Hydrog. Energy* 47 (2022) 41507–41526, <https://doi.org/10.1016/j.ijhydene.2021.12.145>.
- [22] F.R. Shamskar, F. Meshkani, M. Rezaei, Ultrasound assisted co-precipitation synthesis and catalytic performance of mesoporous nanocrystalline NiO-Al<sub>2</sub>O<sub>3</sub> powders, *Ultrason. Sonochem.* 34 (2017) 436–447, <https://doi.org/10.1016/j.ultrsonch.2016.06.021>.
- [23] H.T. Li, Y. Qiu, C. Wang, X. Huang, T.C. Xiao, Y.X. Zhao, Nickel catalysts supported on ordered mesoporous SiC materials for CO<sub>2</sub> reforming of methane, *Catal. Today* 317 (2018) 76–85, <https://doi.org/10.1016/j.cattod.2018.02.038>.
- [24] K.S. Park, J.M. Cho, Y.M. Park, J.H. Kwon, J.S. Yu, H.E. Jeong, J.W. Choung, J. Wook Bae, Enhanced thermal stability of Ni nanoparticles in ordered mesoporous supports for dry reforming of methane with CO<sub>2</sub>, *Catal. Today* 388 (2022) 224–230, <https://doi.org/10.1016/j.cattod.2020.07.016>.
- [25] X.M. Tao, X.X. Li, L. Huang, G.W. Wang, Q.G. Ye, Highly active Ni–Ce/TiO<sub>2</sub>–Al<sub>2</sub>O<sub>3</sub> catalysts: Influence of preparation methods, *Int. J. Hydrog. Energy* 41 (2016) 6271–6276, <https://doi.org/10.1016/j.ijhydene.2016.03.031>.
- [26] Y. Turap, I. Wang, T.T. Fu, Y.M. Wu, Y.D. Wang, W. Wang, Co–Ni alloy supported on CeO<sub>2</sub> as a bimetallic catalyst for dry reforming of methane, *Int. J. Hydrog. Energy* 45 (2020) 6538–6548, <https://doi.org/10.1016/j.ijhydene.2019.12.223>.
- [27] W. Huang, C. Wei, Y. Li, The role of Mo species in Ni–Mo catalysts for dry reforming of methane, *Phys. Chem. Chem. Phys.* 24 (2022) 21461–21469, <https://doi.org/10.1039/D2CP02120J>.
- [28] Z. Song, Q. Wang, C. Guo, S. Li, W.J. Yan, W.Y. Jiao, L. Qiu, X.L. Yan, R.F. Li, Improved effect of Fe on the stable Ni-Fe/Al<sub>2</sub>O<sub>3</sub> catalyst in low-temperature dry reforming of methane, *Ind. Eng. Chem. Res.* 59 (2020) 17250–17258, <https://doi.org/10.1021/acs.iecr.0c01204>.
- [29] T. Margossian, K. Larmier, S.M. Kim, F. Krumeich, C. Müller, C. Copéret, Supported Bimetallic NiFe nanoparticles through colloid synthesis for improved dry reforming performance, *ACS Catal.* 7 (2017) 6942–6948, <https://doi.org/10.1021/acscatal.7b02091>.
- [30] A. Djaidja, H. Messaoudi, D. Kaddeche, A. Barama, Study of Ni–M/MgO and Ni–M–Mg/Al (M=Fe or Cu) catalysts in the CH<sub>4</sub>–CO<sub>2</sub> and CH<sub>4</sub>–H<sub>2</sub>O reforming, *Int. J. Hydrog. Energy* 40 (2015) 4989–4995, <https://doi.org/10.1016/j.ijhydene.2014.12.106>.
- [31] X.D. Liu, L. Li, H.X. Sun, G.M. Wen, D. Wang, S.Y. Ren, Q.X. Guo, W.C. Zhang, S. B. He, B.J. Shen, NiW catalyst modified with C12A7-H<sup>+</sup> and its promotion to hydrogenation selectivity of hydrodesulfurization, *Fuel* 290 (2021), 120037, <https://doi.org/10.1016/j.fuel.2020.120037>.
- [32] T.G. de Araújo Moreira, J.F.S. de Carvalho Filho, Y. Carvalho, J.M.A.R. de Almeida, P.N. Romani, E.F. Sousa-Aguiar, Highly stable low noble metal content rhodium-based catalyst for the dry reforming of methane, *Fuel* 287 (2021) 119536, <https://doi.org/10.1016/j.fuel.2020.119536>.
- [33] C.F. Wu, L.Z. Wang, P.T. Williams, J. Shi, J. Huang, Hydrogen production from biomass gasification with Ni/MCM-41 catalysts: influence of Ni content, *Appl. Catal. B Environ.* 108 (2011) 6–13, <https://doi.org/10.1016/j.apcatb.2011.07.023>.
- [34] D.P. Liu, X.Y. Quek, W.N.E. Cheo, R. Lau, A. Borgna, Y.H. Yang, MCM-41 supported nickel-based bimetallic catalysts with superior stability during carbon dioxide reforming of methane: effect of strong metal–support interaction, *J. Catal.* 266 (2009) 80–90, <https://doi.org/10.1016/j.jcat.2009.07.004>.
- [35] Y.S. Cho, J.C. Park, B. Lee, K.Y. Younghun, J. Yi, Preparation of mesoporous catalyst supported on silica with finely dispersed Ni particles, *Catal. Lett.* 81 (2002) 89–96, <https://doi.org/10.1023/A:1016068324731>.
- [36] B.S. Liu, Z.Y. Wan, Y.P. Zhan, C.T. Au, Desulfurization of hot coal gas over high-surface-area LaMeOx/MCM-41 sorbents, *Fuel* 98 (2012) 95–102, <https://doi.org/10.1016/j.fuel.2012.03.048>.
- [37] E. Savuto, R.M. Navarro, N. Mota, A. Di Carlo, E. Bocci, M. Carlini, J.L.G. Fierro, Steam reforming of tar model compounds over Ni/Mayenite catalysts: effect of Ce addition, *Fuel* 224 (2018) 676–686, <https://doi.org/10.1016/j.fuel.2018.03.081>.
- [38] C. Dueso, A. Abad, F. García-Labiano, L.F. Diego, P. Gayán, J. Adánez, A. Lyngfelt, Reactivity of a NiO/Al<sub>2</sub>O<sub>3</sub> oxygen carrier prepared by impregnation for chemical-looping combustion, *Fuel* 89 (2010) 3399–3409, <https://doi.org/10.1016/j.fuel.2010.03.043>.
- [39] C.K.S. Choong, Z. Zhong, L. Huang, Z. Wang, T.H. Ang, A. Borgna, J.Y. Lin, L. Hong, L.W. Chen, Effect of calcium addition on catalytic ethanol steam reforming of Ni/Al<sub>2</sub>O<sub>3</sub>: I. Catalytic stability, electronic properties and coking mechanism, *Appl. Catal., A* 407 (2011) 145–154, <https://doi.org/10.1016/j.apcata.2011.08.037>.
- [40] P. Xu, Z.M. Zhou, C.J. Zhao, Z.M. Cheng, Ni/CaO–Al<sub>2</sub>O<sub>3</sub> bifunctional catalysts for sorption-enhanced steam methane reforming, *AIChE J.* 60 (2014) 3547–3556, <https://doi.org/10.1002/aic.14543>.
- [41] A.D. Giuliano, K. Gallucci, P.U. Foscolo, C. Courson, Effect of Ni precursor salts on Ni-mayenite catalysts for steam methane reforming and on Ni–CaO-mayenite materials for sorption enhanced steam methane reforming, *Int. J. Hydrog. Energy* 44 (2019) 6461–6480, <https://doi.org/10.1016/j.ijhydene.2019.01.131>.
- [42] S. Dmyanova, B. Pawelec, K. Arishtirova, MCM-41 supported PdNi catalysts for dry reforming of methane, *Appl. Catal., B* 92 (2009) 250–261, <https://doi.org/10.1016/j.apcatb.2009.07.032>.
- [43] D. Kang, H.S. Lim, M. Lee, J.W. Lee, Syngas production on a Ni-enhanced Fe<sub>2</sub>O<sub>3</sub>/Al<sub>2</sub>O<sub>3</sub> oxygen carrier via chemical looping partial oxidation with dry reforming of methane, *Appl. Energy* 211 (2018) 174–186, <https://doi.org/10.1016/j.apenergy.2017.11.018>.
- [44] M. Li, A.C.T. van Veen, Tuning the catalytic performance of Ni-catalysed dry reforming of methane and carbon deposition via Ni–CeO<sub>2-x</sub> interaction, *Appl. Catal., B* 237 (2018) 641–648, <https://doi.org/10.1016/j.apcatb.2018.06.032>.
- [45] B.M. Al-Swai, N. Osman, M.S. Alnarabiji, A.A. Adesina, B. Abdullah, Syngas production via methane dry reforming over ceria–magnesia mixed oxide-supported nickel catalysts, *Ind. Eng. Chem. Res.* 58 (2019) 539–542, <https://doi.org/10.1021/acs.iecr.8b03671>.
- [46] B. Li, T. Mei, S. Du, W.W. Zhang, Synthesis of Ni–Fe and Ni–Fe/ZrO<sub>2</sub> composite coating and evaluation of its structural and corrosion resistance, *Mater. Chem. Phys.* 243 (2020), 122595, <https://doi.org/10.1016/j.matchemphys.2019.122595>.
- [47] T. Dong, J. Li, F. Huang, L. Wang, J. Tu, Y. Torimoto, M. Sadakata, Q.X. Li, One-step synthesis of phenol by O<sup>•</sup> and OH<sup>•</sup> emission material, *Chem. Commun.* 21 (2005) 2724–2726, <https://doi.org/10.1039/b419206k>.
- [48] C. Sprung, B. Arstad, U. Olsbye, Methane steam reforming over a Ni/NiAl<sub>2</sub>O<sub>4</sub> model catalyst-Kinetic, *ChemCatChem* 6 (2014) 1969–1982, <https://doi.org/10.1002/cctc.201402017>.
- [49] J.M. Kolbe, M. Fayaz, A. Sayari, Understanding the effect of water on CO<sub>2</sub> adsorption, *Chem. Rev.* 121 (2021) 7280–7345, <https://doi.org/10.1021/acs.chemrev.0c00762>.
- [50] X. Ma, Y. Li, W. Zhang, Z.Y. Wang, J.L. Zhao, DFT study of CO<sub>2</sub> adsorption across a CaO/Ca<sub>12</sub>Al<sub>14</sub>O<sub>33</sub> sorbent in the presence of H<sub>2</sub>O under calcium looping conditions, *Chem. Eng. J.* 370 (2019) 10–18, <https://doi.org/10.1016/j.cej.2019.03.176>.
- [51] P. Yang, L.B. Duan, H.J. Tang, C.T. Cai, Z. Sun, Explaining steam-enhanced carbonation of CaO based on first principles, *Greenh. Gases: Sci. Technol.* 8 (2018) 1110–1123, <https://doi.org/10.1002/ghg.1822>.
- [52] J.J. Guo, H. Lou, X.M. Zheng, The deposition of coke from methane on a Ni/MgAl<sub>2</sub>O<sub>4</sub> catalyst, *Carbon* 45 (2007) 1314–1321, <https://doi.org/10.1016/j.carbon.2007.01.011>.
- [53] S.M. Kim, P.M. Abdala, T. Margossian, D. Hosseini, L. Foppa, A. Armutlulu, W. A. Beek, A. Comas-Vives, C. Müller, Cooperativity and dynamics increase the performance of NiFe dry reforming catalysts, *J. Am. Chem. Soc.* 139 (2017) 1937–1949, <https://doi.org/10.1021/jacs.6b11487>.